A novel geometry optimization approach for multi-recess hydrostatic bearing pad operating in static and low-speed conditions using CFD simulation

Michal Michalec (michal.michalec@vut.cz)
Brno University of Technology
Martin Ondra
Brno University of Technology
Martin Svoboda
Brno University of Technology
Jiří Chmelík
Brno University of Technology
Petr Zeman
Brno University of Technology
Petr Svoboda
Brno University of Technology
Robert Jackson
Auburn University

Research Article

Keywords: Hydrostatic lubrication, computational fluid dynamics, model validation, optimization methodology

Posted Date: January 6th, 2023

DOI: https://doi.org/10.21203/rs.3.rs-2439009/v1

Version of Record: A version of this preprint was published at Tribology Letters on April 6th, 2023. See the published version at https://doi.org/10.1007/s11249-023-01726-3.

Abstract

This study investigates a new two-parameter method for estimating optimal hydrostatic bearing pad proportions. The design of a hydrostatic bearing pad is limited to simple geometry using analytical equations or one-parameter optimization based on experimental data. In this study, 3D static CFD model results were verified using analytical results and experimental data on a hydrostatic bearing testing device. The obtained CFD results for load and pressure show a deviation within 5.2% compared to the experimentally obtained results and the literature. Using the proposed novel two-parameter optimisation, the energetic loss was reduced by 30% compared to the classical one-parameter approach. This methodology allows versatile and effective design of optimal hydrostatic bearings operating in low-speed conditions to achieve minimum energetic loss.

1. Introduction

Hydrostatic (HS) bearings are a vital part of high-precision machines whose sizes range from millimetres up to tens of metres [1]. They are widely used in machining centres, guideways, turntables, space telescopes and hydro-energetics [2–5]. The main advantages are operation at zero speed, very low friction, minimal wear, high stiffness, and good damping ability. The possibility to operate at zero speed creates a huge advantage for the operation of hydrodynamic bearings in low-speed conditions. Thus, they are frequently combined with HS bearings to improve the performance and reduce wear during low-speed operation and start and stop phases [6, 7]. Such bearings are called hybrid bearings. On the contrary, it is necessary to continuously supply the bearing with pressurized lubricant to maintain a uniform lubricating layer and proper function. The energetic requirements and initial costs are considerably higher than for other bearing types. Nevertheless, interest in replacing large rotors rolling bearings has been rising in recent years to reduce downtime and maintenance costs [8].

The working principle is shown in Fig. 1. Lubricant is supplied by a hydraulic circuit into the recesses of the pad. The generated pressure then lifts the load and separates the solid bodies of the bearing pad and turntable (in case of circular bearings) or slider (in case of guideways). Then, a thick lubricating film of thickness usually in the range of 10–100 μm is created. The lubricant outflowing from the narrow gap is returned to the hydraulic circuit. The restrictor plays an important role in achieving high stiffness, stability, and control. Many types of such devices have been proposed to improve the bearing performance, such as orifice [9, 10], membrane members [11], or feedback systems [12]. The lubricant supply is necessary for proper function while moving or until the required sliding speed is reached, in the case of hybrid bearings, for the hydrodynamic effect to occur and carry the load. Liu et al. [13] concluded, that HS bearings have had an increasing trend of research interest over the last few years. Therefore, it is crucial to design the HS bearing pad for the best performance, and minimal energetic demands, which are increasing with the size of the bearing. He and Wang [14] added that the implementation of the best available technology in the industry can reduce the total energy consumption in some fields by up to 20%, which is a significant amount of energy directly affecting the environment and the final product or service price.

The geometry of the hydrostatic bearing is one of the key parameters that affect the lubricant pressure distribution and the bearing resulting performance [15]. Loeb and Rippel [16] introduced the determination of the optimal pad shape using an electric field plotter analogy [17], where the optimal shape can be determined using performance factors for a variety of pad shapes using experimentally obtained curves. Subsequently, Rippel [18] published a design manual for HS bearings. Khonsari and Booser [19] published a book dealing with tribological aspects in engineering applications, including hydrostatic bearing shape optimization based on Loeb and Rippel [16] methodology. Based on previous research, Bassani and Piccigallo [20] presented a comprehensive methodology for the design of HS bearings describing the most important parameters and design considerations. Chikurov [21] later continued modelling HS bearings using the electric field analogy for possible simplification. A very important step in the HS bearing design process is optimization to achieve the best performance and reduce energetic demands as much as possible [22, 23]. This is especially crucial in large-scale HS bearings, where the energy consumption is significant [24]. To achieve the best performance and stability, a multicriteria optimization approach should be considered [25]. Simple pad geometries, such as circular pads and recesses, have been analytically derived [19]. However, in cases of complex and multi-recess pads, the analytical solution becomes very complicated, and the performance characteristics must be obtained experimentally or using a numerical approach.

Computational Fluid Dynamics (CFD) has been increasingly used in various applications over the past decade. One of the key advantages of this method is that it allows one to obtain many parameters and investigate flow characteristics in areas where it is extremely difficult or even impossible to implement sensors or use optical methods. CFD has already been used to study hydrodynamic, HS, and hybrid bearings [26–28]. Sharma et al. [29] conducted a numerical study to determine the performance of unconventional hybrid bearings. It has been shown, that hybrid bearings perform with lower pressure and temperature peaks, which leads to higher bearing stability [30, 31]. However, it is crucial to determine the accuracy of the model. Cui et al. [32] investigated heavy HS bearing using a quarter CFD model and obtained errors under 10% compared to analytical approaches. Gao and colleagues [10] studied the effect of orifice length in HS bearings and compared the CFD model with experiments that reached errors under 1%. The experiments are crucial to CFD model validation, especially in cases where exact analytical approaches cannot be used. Wasilczuk et al. [33] concluded that the presence of HS pockets in hydrodynamic bearings reduces the temperature change and pressure peaks, leading to higher stability of operation. The drawback of the presence of the pocket is the larger friction losses due to the cooler oil. Wodtke et al. [34] carried out experimental validation for theoretical calculations and predictions of large hydrodynamic thrust bearings and emphasized the necessity of experimental validation of numerical simulations, which are simplified and thus do not represent the real geometry and other influential effects. Helene et al. [35] conducted a parametric study of the flow pattern in the 2D recess of a hybrid bearing based on Navier-Stokes equations with the comparison of laminar and turbulent flow regimes. The authors concluded that the modelling of the turbulent flow regime could contribute to better understanding of the inertia and viscous effects in recess bearings. For that reason, turbulent models were later used by Ghezali et al. [36] and Gao et al. [10] in hydrostatic bearing orifice performance numerical investigation. Horvat and Braun [37] extended the study of numerical flow characteristics to 3D HS journal bearings with experimental validation using laser flow visualisation of streamline maps at a high rotational speed. A similar study was later conducted on HS thrust bearings to investigate geometric patterns and different pad shapes, concluding that the presented model may be useful in HS bearing load carrying capacity and stiffness of HS bearings for low-speed applications [38]. Du et al. [39] proposed an analytical model for the analysis of the pressure of tilted HS journal bearings validated using a CFD and experimental procedure. Guo et al. [40] performed a comparison of CFD codes for static and dynamic properties in hydrodynamic and HS bearing applications. The authors agree that CFD will play an important role in bearing and damper analysis in future research. The comparison of CFD standard code to a special one made for HS, hydrodynamic any hybrid bearing analyses showed good agreement, which leads to a conclusion that general codes might be used for the investigation of such bearings and their static and dynamic characteristics.

The CFD can significantly speed up the development, reduce costs, and provide detailed information about the flow character and many parameters. Although the CFD approach is widely adopted in various applications, including HS, hydrodynamic and hybrid bearings, it is necessary to set appropriate boundary conditions and verify the results obtained with an experimental approach [41–43]. Moreover, many papers dealing with CFD analyses of HS bearings have been proposed over the last years, although only a few of them offered practical design recommendations. This article aims to optimize recess size and position in HS bearing pads to minimize energetic loss while achieving the best performance for static and low-speed conditions. The presented geometry optimization multi-parameter approach using area ratio and recess position has not yet been proposed.

NOMENCLATURE		
Symbol	**Description**	**Unit**
W	Bearing load	N
A_{tot}	Total pad area	mm^2
A_r	Total recess area	mm^2
a	Recess radius	mm
D	Recess diameter	mm
l	Quarter model edge length	mm
t	Recess position from pad centre	mm
h	Film thickness	mm
H_f	Power loss factor	$-$
Q_f	Flow factor	$-$
P_f	Load factor	$-$
P_r	Recess pressure	MPa
P_{atm}	Atmospheric pressure	MPa
Q	Supplied flow	$\mathrm{L/min}$
μ	Dynamic viscosity of lubricant	$\mathrm{Pa} \bullet \mathrm{s}$
η	Pump efficiency	$-$

2 Materials And Methods

Three approaches were used to verify the obtained results - analytical, experimental and CFD. An integrated process was also followed to create and analyse the results using these three methods, as shown in Fig. 2. Based on the analytical calculation, experimental conditions were determined. Afterwards, boundary conditions of the CFD analysis were set according to the resulting analytical results and experimental conditions. Subsequently, all results were compared and discussed.

2.1 Analytical approach

Navier-Stokes equations play a significant role in the field of fluid mechanics. Nonetheless, due to the complexity of the Navier-Stokes equations, it is almost impossible to obtain analytical expressions to calculate required flow characteristics. Therefore, certain assumptions can be considered to help to obtain a simpler form of equations. The assumptions are as follows:

1. Film thickness is constant and small compared to its size in other directions.
2. The fluid is Newtonian, incompressible and isoviscous.
3. Inertia terms are negligible compared to the viscous forces.
4. No squeeze nor sliding exists, and the bearing surfaces are stationary.
5. The pressure of lubricant is constant in the direction of the film thickness $(\partial p/\partial z = 0)$.
6. There Is A Continuous Supply Of Lubricant, And The Flow Is Laminar.

Then the Reynolds equation for computation of the pressure distribution in the simplified form is as follows:

$$\frac{\partial}{\partial x}\left(\frac{h^3}{12\mu}\frac{\partial p}{\partial x}\right)+\frac{\partial}{\partial y}\left(\frac{h^3}{12\mu}\frac{\partial p}{\partial y}\right)=0$$

1

After obtaining the pressure distribution, the load-carrying capacity (or acting force) can be expressed as:

$$W = P_r \bullet A_{eff}$$

2

where P_s is recess pressure and A_{eff} is effective area of the pad, which can be expressed from effective pad area proportion β ($\beta < 1$) and total area of the pad A_{tot}:

$$A_{eff} = \beta \bullet A_{tot}$$

3

The equations (1–3) can be further customized and utilized to express required flow supply to the bearing as follows:

$$Q = Q_f \frac{W}{A_{tot}} \frac{h^3}{12 \bullet \mu}$$

4

where h is film thickness, μ is dynamic viscosity of lubricant, and Q_f is flow factor, dependent on the geometry and the effective area of the bearing.

Loeb [17] introduced a new methodology for estimating optimal proportions of the bearing pad and recess based on electric analog field plotter. Generalized analytical equations could be used to calculate the bearing performance using read values obtained from graphs, presented in Loeb and Rippel [16]. Similarly, the performance factors (Eq. 5–7), can be determined based on known values of bearing characteristics.

a) pressure factor $P_f = \frac{P_r}{W} \bullet A_{tot}$ (5)

b) flow factor $Q_f = \frac{12 \bullet \mu}{W \bullet h^3} \bullet Q \bullet A_{tot}$ (6)

c) power loss factor $H_f = \frac{P_f \bullet Q_f}{\eta}$ (7)

The equations (5,6) can be transformed to obtain the required variable from the expression. An example of designing a HS bearing pad proportions using one-parameter optimization is shown in Fig. 3. The ratio *(a/l)* represents the characteristic dimension of the recess to the characteristic dimension of the pad, that is, the diameter of the recess to the pad edge length. One primary parameter is kept constant (usually recess size to retain the required lifting area), while the other is optimized. The aim of the pad geometry optimization is generally to achieve the best possible performance with minimal pumping power loss, in this case, the power loss factor – H_f. And for the *(a/l)* ratio of the minimum power loss factor, the values of optimal pressure (P_f) and flow (Q_f) factors are obtained, respectively.

In the basic approach, only one of the two parameters: *a* or *l*, are used, while the recess position *(t = l)*, is assumed. The optimization approach using performance curves in a 2D graph utilizes *(l = 4a)*. However, we defined the new variable parameter *(t)* to describe the position of the recess. Thus, the proposed method uses two-parameter criteria, recess position *(t)*, and recess area to total pad area ratio (A_r/A_{tot}), for performance optimization. The area and the position of the recess were chosen as the primary parameters because the recess shapes may be chosen to better accommodate the pad shape and thus improve the bearing performance. The length of the edge of the pad *(2l)* remained constant, so the second variable assumed in this study was the recess radius – *a*. Attention should be paid to prevent exceeding the recess area out of the pad geometry, i.e., in case the pad has rounded corners, etc.

Table 1
Performance factors for experimental pad proportions read from Fig. 4 *of* [16]

Parameter	Label	Value
Pressure factor	P_f	1.52
Flow factor	Q_f	27.4
Power loss factor	H_f	41.65

2.2 Experimental validation

2.2.1 Lubricant viscosity

To obtain all the inputs required to build a relevant mathematical model, the dynamic viscosity measurement was performed on a rotational viscometer HAAKE RotoVisco® 1 (PSL Systemtechnik, Germany) rotational viscometer. Measured data was filtered with 99.88% reliability using a Bingham rheological model. The dynamic viscosity of the used ISO VG 46 grade hydraulic oil was fitted using the Vogel-Fulcher equation with R^2 = 99.89%. The experiments were carried in static conditions, with stable temperature 23°C recorded using temperature sensors in the recess. The results shown very low temperature difference throughout the measurements, only ± 1°C. Thus, constant viscosity of 0.104 Pa•s was considered in all simulations. It has been previously observed by Schmelzer et al. [44] that the pressure-viscosity dependence of liquids of constant composition is extremely small (around 2%) in the investigated pressure range (0–1 MPa). Therefore, the pressure-viscosity dependence was neglected in this study.

2.2.2 Two-pad HS experimental bearing (2-PAD)

The experimental device used to obtain the measured data for evaluation is schematically shown in Fig. 4. It consists of two main parts, the bearing, and the hydraulic circuit, which supplies pressurized lubricant with a pump powered by an electromotor. The hydraulic circuit is equipped with safety features such as a check valve and a pressure relief valve. The hydraulic accumulator minimizes the pressure spikes generated by the pump. The flowmeter measures the total supplied flow to the whole bearing. Flow restrictors (throttle valves), secure bearing stability in the event of asymmetrical load or misalignment. A pressure sensor of 0.25 bar precision is mounted on each of the inlets to the recess. The lubricant that flows out of the contact area to the collector is returned to the oil tank.

Three contact potentiometer proximity sensors are mounted on each of the 2-PAD pads for obtaining film thickness with precision of 0.01 mm and range of 3 mm. To measure the actual temperature in the recess area, a thermometer is fitted in each of the recesses for calculation of the viscosity value of the lubricant. The load is created using four set screws, each mounted with a load cell with ± 5 N precision, which provides a real-time measurement of the loading force. The experimental measurements were carried out three times after the temperature in the recess area stabilized at 23°C (corresponding to a dynamic viscosity of 0.104 Pa s). Since the hydraulic circuit has relatively large tank (100 liter), no additional cooling was necessary. The experimental conditions were based on the previous test bearing comparison with analytical equations in ref. [45]. The total supplied flow into both of the pads was set to 8.5 l/min. A comparison of predicted and measured film thickness with variable load was presented in reference [45], where the highest precision was achieved at 16 kN load. Therefore, for all measurements, a total load of 16 kN was applied in this study. The resulting average film thickness was 0.197 mm. The pad size used in experiments was 140x140 mm with recess diameters of 35 mm and positions of t = 35 mm. Inlet hole diameter was 12 mm, and recess depth was 5 mm.

2.3 Numerical approach

CFD analysis has become a favoured method for the analysis of fluid dynamics. It provides a detailed understanding of the lubricant flow in hydrostatic bearings. In this study, the CFD analysis was done using commercial software ANSYS Fluent 2021 R2 based on the Finite Volume Method with Cell-Centered formulation. The code solves the conservation equations for mass (Eq. 8) and momentum (Eq. 9), respectively.

$$\nabla \bullet v = 0$$

8

$$\boxed{\rho \left(v \bullet \nabla\right) v = -\Delta p + \mu \nabla^2 v \qquad (9)}$$

In this case, pressure-based steady-state incompressible flow with absolute velocity formulation was investigated without considering thermal effects and gravity. A uniform lubricant film was considered in all simulations. Because relatively high film thickness and low pressure were assumed for very short experimental tests isothermal conditions were assumed – constant viscosity (0.104 Pa s) and density (875 kg/m^3) were established for all simulation design points. As indicated in the previous research papers, turbulent models were used in HS bearing simulations to improve the obtained results with considering the influence of vortices emerging in the recess area. Moreover, the previous research [35–37], as well as preliminary simulation results showed better agreement of the predicted results for turbulent model k-ω SST than for the laminar viscous model. Therefore, k-ω SST viscous model with 5% turbulent intensity and turbulent viscosity ratio of 10 was used for all simulations. The operating conditions included an atmospheric pressure of 101.3 kPa to reflect the real conditions. The 3D geometry of the fluid domain was parametrized in 3D modelling software of the program. The variable parameters, recess position and diameter, are listed in Table 2. The simulation of all design points was conducted using the setting described below.

Table 2
Combination table of variable parameters for simulation design points

Area ratio A_r/A_{tot} **(-)**	**0.05**	**0.1**	**0.2**	**0.3**	**0.4**	**0.5**	**0.6**	**0.7**	**0.75**
Recess diameter ***D (mm)***	**17.66**	**24.98**	**35.32**	**43.26**	**49.96**	**55.85**	**61.18**	**66.08**	**68.40**
Recess position *t (mm)*	8.83	12.48	17.66	21.63	24.97	27.92	30.59	33.04	34.20
	19.29	21.49	24.59	26.97	28.98	30.75	32.35	33.82	34.52
	29.76	30.49	31.53	32.32	32.99	33.58	34.12	34.61	34.84
	40.23	39.50	38.46	37.67	37.01	36.41	35.88	35.39	35.16
	50.70	48.50	45.40	43.02	41.01	39.24	37.64	36.17	35.48

The fluid domain of one quarter of the pad was discretized into a polyhedral mesh in built-in ANSYS Fluent Meshing (Fig. 6). The target mesh size in the upper plane and the lubricating film regions was set to 0.128 μm to enhance the results of the forces acting in the upper plane. A mesh sensitivity analysis was performed with the same boundaries as in the final analysis to determine the mesh quality and stability (Fig. 7). An approximate number of polyhedral elements, 1e + 07, was used in all simulations with average maximum skewness 0.4 and minimal orthogonality of 0.35. Six boundary layers were added to the walls in the recess region, and four in the inlet region, to enhance near wall fluid behaviour. The number of boundary layers was established according to preliminary simulations. The resulting wall Y + value along the top surface was in the range from 0.12 to 0.18. However, the precision of the model was primarily judged according to the analytically predicted and experimentally obtained results. There is no limitation for the film thickness range, but lower film thicknesses may require longer computational times to secure smooth mesh element transition from the recess area to the film region.

Hydrostatic bearings are usually modelled only with the part of the inlet region directly flowing to the recess. However, the initial comparison of the fluid domain only with straight vertical pipe showed a bigger difference to experimental data. Therefore, the fluid domain was modelled with the inlet region to the location of the pressure sensor location on the experimental rig. For all simulations, a uniform film thickness of 0.197 mm, as obtained from experimental measurements, was used for all design points. The boundary conditions can be seen in Fig. 8. Starting with the mass flow inlet (Q) set at 7.096E-5 m^3/s, symmetry conditions were employed on the symmetry planes of the quarter model and pressure outlet with atmospheric pressure operating condition (P_{atm}). Output parameters were the resulting force on the top plane of the bearing and average pressure over the recess area.

The residuals of continuity and momentum equations condition were set below 10^{-4} to achieve convergence. Underrelaxation factors for both velocity and pressure, were set at 0.5 and 0.5, respectively, without any further need for adjustment. We used the coupled pressure-velocity coupling scheme, which should provide robust and high performance for steady-state flows compared to the segregated schemes available in ANSYS Fluent. The gradient least squares-based spatial discretization method was used. The first-choice schemes – second order, and second order upwind were kept for pressure and momentum, respectively. Hybrid initialization was conducted to improve the convergence. One case of the calculation took approximately 2 hours with the used computer specifications: 12 physical cores of 3,47 GHz processor, 96 GB of RAM, and 1 TB SSD to store retained case data.

3. Results And Discussion

Firstly, the comparison of results obtained from experiments, calculations, and CFD simulations were performed to validate the CFD model precision. The total load applied per pad was obtained using load cells. The experimental measurements were performed three times with a resulting average deviation within 0.5%. The calculated load was obtained using information from sensors mounted on the pad. Then, a 3D CFD model was created and computed. The results are shown in Fig. 9 for recess pressure and in Fig. 10 for load. The experimental results show relatively good agreement with the calculation considering the precision of the used sensors. The weight of slider and loading frame was included in load evaluation. The difference in results of recess pressure compared to the experiments reached 8.1% for calculation and 4.2% for the CFD analysis. The CFD results for the load were obtained from resulting force acting on the top (contact) plane of the model. The obtained difference in load was 5.2% and 2.3% for experimental results and for calculation, respectively. Considering the recess pressure in the pad, the experimental results show good agreement with those obtained from CFD simulation. The differences that emerged could have been mainly caused by the sensor precision of the experimental device and the CFD model precision. A dominant effect could be caused by the dynamic viscosity variation with temperature, which approximately changes by 5% for 1°C. Nonetheless, a constant viscosity was used for all simulations to determine optimal geometry, so that the comparison of various shapes was unaffected. A minor contribution to the results difference could be caused by the geometry imperfections of the HS bearing (surface flatness and roughness), or the recess depth effect influence, which is in the case of analytical calculation neglected. The obtained results clearly indicated that the proposed approach could be used for further performance investigation and optimization of performance.

After conducting the initial comparison of the different approaches, the numerical CFD study was solved for all the design points from Table 2. The performance factors P_f, Q_f and H_f were calculated from the results obtained using equations (5–7) for all design points. The results of all performance factors are shown in Fig. 11-Figure 13 in the form of a) 3D graphs with the variable recess on the y-axis and variable area ratio on the x-axis, forming the two-parameter approach, and b) area ratio sections for better readability of the data. The load factor (Fig. 11) shows a similar trend as in the reference experimentally obtained 2D graph from [16]. Generally, the optimization goal is to achieve the lowest P_f, Q_f, and H_f, assuming equations (5–7). The results for the load factor indicate that the load-carrying capacity decreases with increasing area ratio, or position from the origin, separately and together. The lowest value of P_f can be found in the middle sector of the graph. In the case of flow factor (Fig. 12), it is obvious that the larger the area ratio, or the farther the position of the recess from the centre, the higher flow is required to sustain certain film thickness or load-carrying capacity. Therefore, to achieve the lowest energy requirements, a minimal H_f should be considered. Thus, the power loss factor (Fig. 13) expresses the overall performance – to secure an optimum between the highest load capacity and the lowest power requirements (as expressed in Fig. 3). Nevertheless, we emphasize that in the case of open-type bearings (without counter pads, as explained in ref. [1]), the recess position should be chosen, also considering the ability of the bearing to manage asymmetrical loading and pad misalignment. This is another reason why the multi-parameter approach offers a more versatile design process compared to the classical one-parameter approach.

As seen in Fig. 14, we also investigated the pressure contours of the various pad shapes, from smallest and closest to the pad centre, to the farthest and biggest. It is obvious, that the larger the land area (as for the smallest area ratio), the higher the recess pressure. Nonetheless, the load capacity and ability to manage asymmetrical loading and misalignment are not desirable in this case (Fig. 14a). The recess pressure was gradually decreasing with increasing recess size and distance from the pad centre (Fig. 14b). The highest ability to manage asymmetrical loading was achieved with largest recess size (Fig. 14c). The sealing edge is very small in this case and the pressure gradient is the steepest (Fig. 15) for this configuration, which makes the bearing extremely sensitive to pad misalignment. Even though the smallest load factor was obtained, the largest flow factor resulted for this case, which is undesirable.

To determine the optimal shape of the bearing, the minimum power loss factor was searched for. To obtain a more accurate result, the minimum was not chosen from the calculated values of the design points, but by using a cubic interpolated surface as seen in Fig. 16. This step allowed us to look for the minimum value of the power loss factor also between the calculated points. The calculated points were used to fit the cubic interpolated surface with normalization in MATLAB R2021a. It is also possible to use linear interpolation, which is simpler but does not capture the surface trend and curvature as well as the cubic interpolation. Subsequently, a minimum value of the power loss factor was found. Then, the coordinates of the minimum value expressed the optimal shape – the recess position and area ratio, respectively. The minimum value of the power loss factor, 26.65, obtained by CFD simulation was determined for the recess position 24.6 mm from the centre and an area ratio of 0.2. In contrast, optimal value of the power loss factor obtained from the graph presented by Loeb and Rippel [16] is 38, with recess position of 35 mm and area ratio of 0.132. Compared to the basic approach using one-parameter criteria, a 30% reduction of the power loss factor was achieved. The investigated ranges of recess position and area ratio were chosen according to the pad size and computable geometry. The interpolated grid could be finer if even higher precision was required. The deformed grid areas on the left side of the 3D graph in Fig. 16 are only a graphical representation of the grid fitted over the sample points and thus are not evaluated.

Finally, we compared the pressure contours of the optimal shape obtained from the classical approach (Fig. 17a) and the presented two-parameter approach (Fig. 17b), respectively. The classical approach optimization resulted in smaller recess diameter and its farther position from the pad centre compared to the two-parameter approach, which also resulted in higher recess pressure due to larger sealing edge. As can be seen in the comparison of the two pressure contours (Fig. 17), the one-parameter approach performed with pressure decrease in the central area, while the two-parameter approach showed uniform pressure among the four recesses. This has also been observed in all two-parameter approach pressure contours as seen in Fig. 14. The results indicate that the proposed method provides more uniform pressure distribution and contributes to higher bearing load capacity, stiffness, and ability to manage asymmetrical loading and pad misalignment.

4. Conclusions

This paper presents a novel approach to HS multi-recess thrust bearing pad geometry optimization using results based on CFD simulations. Nonetheless, the proposed method can be used for journal HS bearings, and eventually also for hybrid bearing lifting pocket layout and size optimization. The precision of the CFD model was within 5.2% for load and 4.2% for pressure, respectively, compared to the analytical and experimental results. The proposed two-parameter criterion was used to evaluate the optimal shape – recess position and recess area to pad area ratio. The obtained results from two-parameter optimization show a possible 30% power loss factor reduction, which is directly related to pumping power loss, compared to the case of conventionally used one-parameter criterion. Moreover, it has been observed that the position of the recess has a strong influence on the resulting performance, and thus the size and position should be evaluated independently. The pressure contours indicate that the proposed two-parameter method provides more even pressure distribution in the central area of the pad, resulting in higher load capacity, stiffness, and ability to manage asymmetrical loading and pad misalignment. The optimization scheme tailored for best performance at lowest energetic requirements can be used for various shapes with custom defined geometric parameters. The proposed method might bring about a notable reduction in the energetic demands, especially for bearings of large-scale structures. Although in the presented study a cross-symmetrical four recess HS bearing pad geometry was optimized, this approach can be applied to any shape of HS bearing and a wide range of operating conditions – from very low to extremely high loads and recess pressures. It is necessary to determine the area ratio and position of the recess grooves first, then perform CFD analysis of selected design points, and find the minimal power loss factor. The drawback of the presented method is the computational time required to evaluate all design points, which nonetheless, depends on the machine used for simulations.

Further research might aim at full experimental evaluation of the presented 3D optimization graphs. The next steps might lead to the preparation of 3D optimization graphs for the mostly used bearing pad geometries to improve the design process of HS bearings. The precision of the model presented in this article could be further improved by considering the influence of sliding speed and thermal effects, and sliding surface geometric precision (i.e., manufacturing and assembly errors). Very little attention has been paid to the structural deformation of the slider/turntable caused by the pressurized fluid flow. An experimental verification of real effects on bearing performance would provide valuable information for design engineers.

Declarations

Funding

This research was carried out under the project FSI-S-20-6443 with financial support from the Ministry of Education, Youth and Sports of the Czech Republic. Michal Michalec would like to thank Prof. Michel Fillon (University of Poitiers, FR) for assistance and comments that greatly improved the manuscript.

Conflict of interest

The authors reported no potential conflict of interest.

Replication of results

On behalf of all authors, the corresponding author states that the results presented in this paper can be reproduced by the implementation details provided herein. Researchers or interested parties are welcome to contact the authors for further explanation, who may also provide the MATLAB codes under request**.**

References

1. Michalec, M., Svoboda, P., Křupka, I., Hartl, M.: A review of the design and optimization of large-scale hydrostatic bearing systems. Eng. Sci. Technol. an Int. J. (2021). https://doi.org/10.1016/j.jestch.2021.01.010
2. Rowe, W.B.: Advances in hydrostatic and hybrid bearing technology. Proc. Inst. Mech. Eng. Part C J. Mech. Eng. Sci. 203, 225–242 (1989). https://doi.org/10.1243/PIME_PROC_1989_203_110_02
3. Sheehan, M., Gunnels, S., Hull, C., Kern, J., Smith, C., Johns, M., Shectman, S.: Progress on the structural and mechanical design of the Giant Magellan Telescope. Ground-based Airborne Telesc. IV. 8444, 84440N (2012). https://doi.org/10.1117/12.926469
4. Jang, S.-H., Choi, Y.-H., Kim, S.-T., An, H.-S., Choi, H.-B., Hong, J.-S.: Development of Core Technologies of Multi-tasking Machine Tools for Machining Highly Precision Large Parts. J. Korean Soc. Precis. Eng. 29, 129–138 (2012). https://doi.org/10.7736/kspe.2012.29.2.129
5. Liming, Z., Yongyao, L., Zhengwei, W., Xin, L., Yexiang, X.: A review on the large tilting pad thrust bearings in the hydropower units. Renew. Sustain. Energy Rev. 69, 1182–1198 (2017). https://doi.org/10.1016/j.rser.2016.09.140
6. De Pellegrin, D. V., Hargreaves, D.J.: An isoviscous, isothermal model investigating the influence of hydrostatic recesses on a spring-supported tilting pad thrust bearing. Tribol. Int. 51, 25–35 (2012). https://doi.org/10.1016/j.triboint.2012.02.008
7. Bouyer, J., Wodtke, M., Fillon, M.: Experimental research on a hydrodynamic thrust bearing with hydrostatic lift pockets: Influence of lubrication modes on bearing performance. Tribol. Int. 165, 107253 (2022). https://doi.org/10.1016/J.TRIBOINT.2021.107253

8. Dhanola, A., Garg, H.C.: Tribological challenges and advancements in wind turbine bearings: A review. Eng. Fail. Anal. 118, 104885 (2020). https://doi.org/10.1016/j.engfailanal.2020.104885
9. Rajasekhar Nicodemus, E., Sharma, S.C.: Orifice compensated multirecess hydrostatic/hybrid journal bearing system of various geometric shapes of recess operating with micropolar lubricant. Tribol. Int. 44, 284–296 (2011). https://doi.org/10.1016/j.triboint.2010.10.026
10. Gao, S., Shang, Y., Gao, Q., Lu, L., Zhu, M., Sun, Y., Yu, W.: CFD-based investigation on effects of orifice length–diameter ratio for the design of hydrostatic thrust bearings. Appl. Sci. 11, (2021). https://doi.org/10.3390/app11030959
11. Chen, D.C., Chen, M.F., Pan, C.H., Pan, J.Y.: Study of membrane restrictors in hydrostatic bearing. Adv. Mech. Eng. 10, (2018). https://doi.org/10.1177/1687814018799604
12. Rehman, W.U., Yuanxin, L., Guiyun, J., Yongqin, W., Yun, X., Iqbal, M.N., Zaheer, M.A., Azhar, I., Elahi, H., Xiaogao, Y.: Control of an oil film thickness in a hydrostatic journal bearing under different dynamic conditions. Proc. 29th Chinese Control Decis. Conf. CCDC 2017. 5072–5076 (2017). https://doi.org/10.1109/CCDC.2017.7979395
13. Liu, Z.F., Wang, Y.M., Cai, L.G., Zhao, Y.S., Cheng, Q., Dong, X.M.: A review of hydrostatic bearing system: Researches and applications. Adv. Mech. Eng. 9, (2017). https://doi.org/10.1177/1687814017730536
14. He, K., Wang, L.: A review of energy use and energy-efficient technologies for the iron and steel industry. Renew. Sustain. Energy Rev. 70, 1022–1039 (2017). https://doi.org/10.1016/j.rser.2016.12.007
15. Okabe, E.P.: Analytical model of a tilting pad bearing including turbulence and fluid inertia effects. Tribol. Int. 114, 245–256 (2017). https://doi.org/10.1016/j.triboint.2017.04.030
16. Loeb, A.M., Rippel, H.C.: Determination of optimum proportions for hydrostatic bearings. ASLE Trans. 1, 241–247 (1958). https://doi.org/10.1080/05698195808972336
17. Loeb, A.M.: The Determination of the Characteristics of Hydrostatic Bearings through the use of the Electric Analog Field Plotter. A S L E Trans. 1, 217–224 (1958). https://doi.org/10.1080/05698195808972333
18. Rippel, H.: Cast Bronze Hdyrostatic Bearing Design Manual. Cast Bronze Institute, inc., Cleveland (1969)
19. Khonsari, M.M., Booser, R.E.: Applied tribology. (1970)
20. Bassani, R., Piccigallo, B.: HYDROSTATIC LUBRICATION. Tribol. Ser. 22, (1992)
21. Chikurov, N.G.: Modeling of hydrostatic bearings by electrical analogy. Russ. Eng. Res. 37, 517–522 (2017). https://doi.org/10.3103/S1068798X17060107
22. Fedorynenko, D., Sapon, S., Boyko, S., Urlina, A.: Increasing of energy efficiency of spindles with fluid bearings. Acta Mech. Autom. 11, 204–209 (2017). https://doi.org/10.1515/ama-2017-0031
23. Doshi, N., Bambhania, M.: Optimization of Film Thickness for Hydrostatic Circular Pad Bearing Used in V-25 vertical Turning Machine. 118–121 (2013). https://doi.org/10.1453/IJMER/21

24. Li, X., Wang, X., Li, M., Ma, Y., Huang, Y.: The research status and progress of heavy/large hydrostatic thrust bearing. Adv. Mech. Eng. 2014, (2014). https://doi.org/10.1155/2014/982584
25. Solmaz, E., Babalik, F.C., Öztürk, F.: Multicriteria optimization approach for hydrostatic bearing design. Ind. Lubr. Tribol. 54, 20–25 (2002). https://doi.org/10.1108/00368790210415338
26. Kozdera, M., Drbáková, S.: Numerical modelling of the flow in the annular multi-recess hydrostatic thrust bearing using CFD methods. EPJ Web Conf. 45, (2013). https://doi.org/10.1051/epjconf/20134501051
27. Xu, X., Shao, J., Yang, X., Zang, Y., Yu, X., Gao, B.: Simulation on multi-oil-cavity and multi-oil-pad hydrostatic bearings. Appl. Mech. Mater. 274, 274–277 (2013). https://doi.org/10.4028/www.scientific.net/AMM.274.274
28. Snyder, T., Braun, M.: Comparison of perturbed Reynolds equation and CFD models for the prediction of dynamic Coefficients of sliding bearings, (2018)
29. Sharma, S.C., Sinhasan, R., Jain, S.C., Singh, N., Singh, S.K.: Performance of hydrostatic/hybrid journal bearings with unconventional recess geometries. Tribol. Trans. 41, 375–381 (1998). https://doi.org/10.1080/10402009808983761
30. Fillon, M., Wodtke, M., Wasilczuk, M.: Effect of presence of lifting pocket on the THD performance of a large tilting-pad thrust bearing. Friction. 3, 266–274 (2015). https://doi.org/10.1007/s40544-015-0092-4
31. Raud, X., Fillon, M., Helene, M.: Numerical modelling of hydrostatic lift pockets in hydrodynamic journal bearings – Application to low speed working conditions of highly loaded tilting pad journal bearings. Mech. Ind. 14, 327–334 (2013). https://doi.org/10.1051/meca/2013073
32. Cui, C., Guo, T., Wang, Y., Dai, Q.: Research on carrying capacity of hydrostatic slideway on heavy-duty gantry CNC machine. AIP Conf. Proc. 1839, (2017). https://doi.org/10.1063/1.4982524
33. Wasilczuk, M., Wodtke, M., Dabrowski, L.: Field tests on hydrodynamic and hybrid operation of a bidirectional thrust bearing of a pump-turbine. Lubricants. 5, (2017). https://doi.org/10.3390/lubricants5040048
34. Wodtke, M., Schubert, A., Fillon, M., Wasilczuk, M., Pajaczkowski, P.: Large hydrodynamic thrust bearing: Comparison of the calculations and measurements. Proc. Inst. Mech. Eng. Part J J. Eng. Tribol. 228, 974–983 (2014). https://doi.org/10.1177/1350650114528317
35. Helene, M., Arghir, M., Frene, J.: Numerical study of the pressure pattern in a two-dimensional hybrid journal bearing recess, laminar, and turbulent flow results. J. Tribol. 125, 283–290 (2003). https://doi.org/10.1115/1.1537233
36. Ghezali, F., Bouzidane, A., Thomas, M.: 3D Numerical investigation of pressure field of an orifice compensated hydrostatic bearing. Mech. Ind. 18, (2017). https://doi.org/10.1051/meca/2016008
37. Horvat, F.E., Braun, M.J.: Comparative experimental and numerical analysis of flow and pressure fields inside deep and shallow pockets for a hydrostatic bearing. Tribol. Trans. 54, 548–567 (2011). https://doi.org/10.1080/10402004.2011.575535

38. Shen, F., Chen, C.L., Liu, Z.M.: Effect of Pocket Geometry on the Performance of a Circular Thrust Pad Hydrostatic Bearing in Machine Tools. Tribol. Trans. 57, 700–714 (2014). https://doi.org/10.1080/10402004.2014.906694
39. Du, Y., Mao, K., Liu, H., Mao, X., Li, Z.: A simplified analytical method for the pressure of tilt hydrostatic journal bearing. Ind. Lubr. Tribol. 70, 993–1001 (2018). https://doi.org/10.1108/ILT-03-2017-0077
40. Guo, Z., Hirano, T., Kirk, R.G.: Application of CFD analysis for rotating machinery - Part I: Hydrodynamic, hydrostatic bearings and squeeze film damper. J. Eng. Gas Turbines Power. 127, 445–451 (2005). https://doi.org/10.1115/1.1807415
41. Shao, J. peng, Liu, G. dong, Yu, X.: Simulation and experiment on pressure field characteristics of hydrostatic hydrodynamic hybrid thrust bearings. Ind. Lubr. Tribol. 71, 102–108 (2019). https://doi.org/10.1108/ILT-02-2018-0063
42. Childs, D.W., Esser, P.: Measurements Versus Predictions for a Hybrid (Hydrostatic Plus Hydrodynamic) Thrust Bearing for a Range of Orifice Diameters. J. Eng. Gas Turbines Power-Transactions Asme. 141, (2019). https://doi.org/10.1115/1.4042721
43. Fesanghary, M., Khonsari, M.M.: On the optimum groove shapes for load-carrying capacity enhancement in parallel flat surface bearings: Theory and experiment. Tribol. Int. 67, 254–262 (2013). https://doi.org/10.1016/j.triboint.2013.08.001
44. Schmelzer, J.W.P., Zanotto, E.D., Fokin, V.M.: Pressure dependence of viscosity. J. Chem. Phys. 122, (2005). https://doi.org/10.1063/1.1851510
45. Michalec, M., Polnický, V., Foltýn, J., Svoboda, P., Šperka, P., Hurník, J.: The prediction of large-scale hydrostatic bearing pad misalignment error and its compensation using compliant support. Precis. Eng. 75, 67–79 (2022). https://doi.org/10.1016/j.precisioneng.2022.01.011

Figures

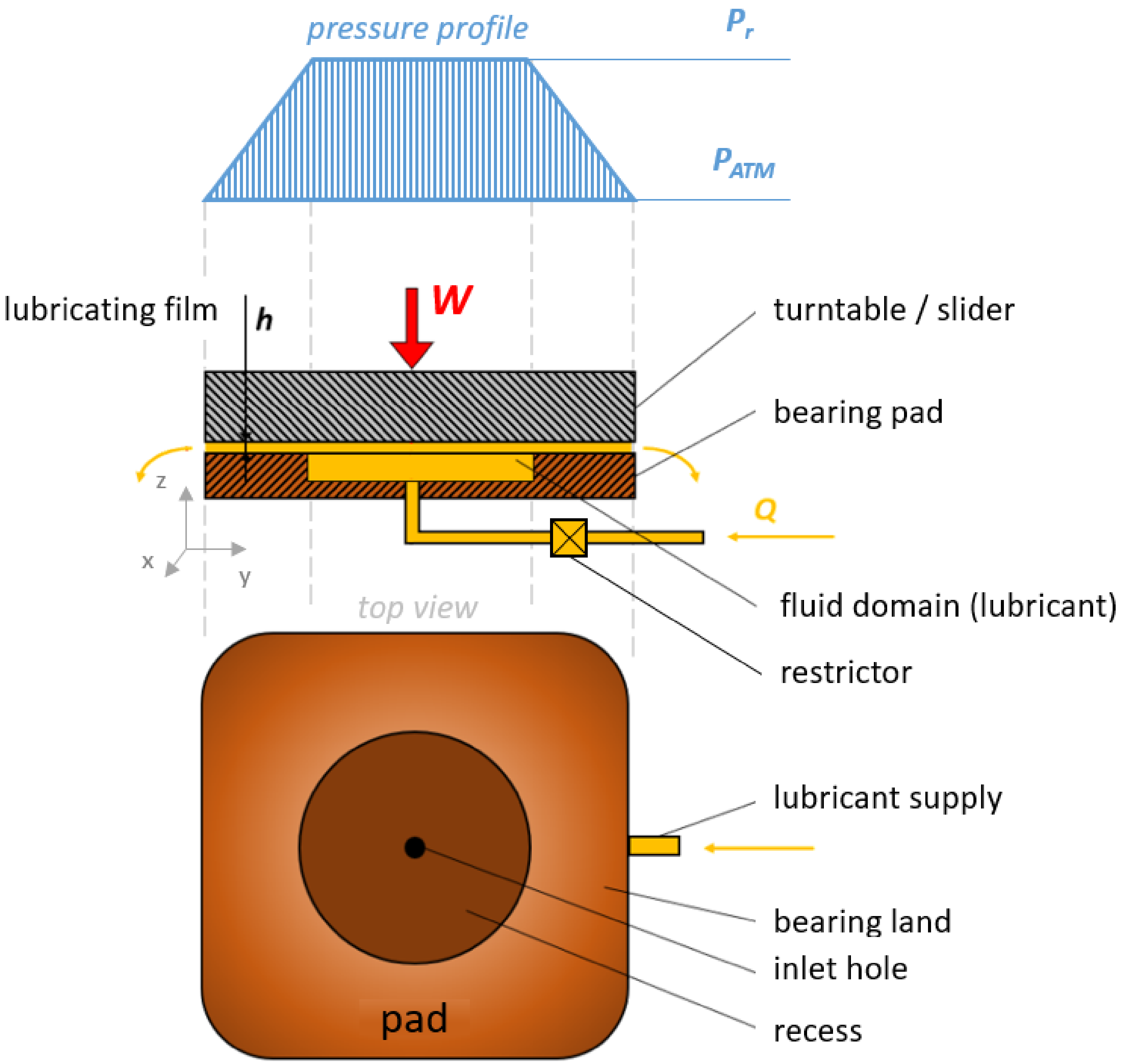

Figure 1

Scheme of the bearing parts and working principle

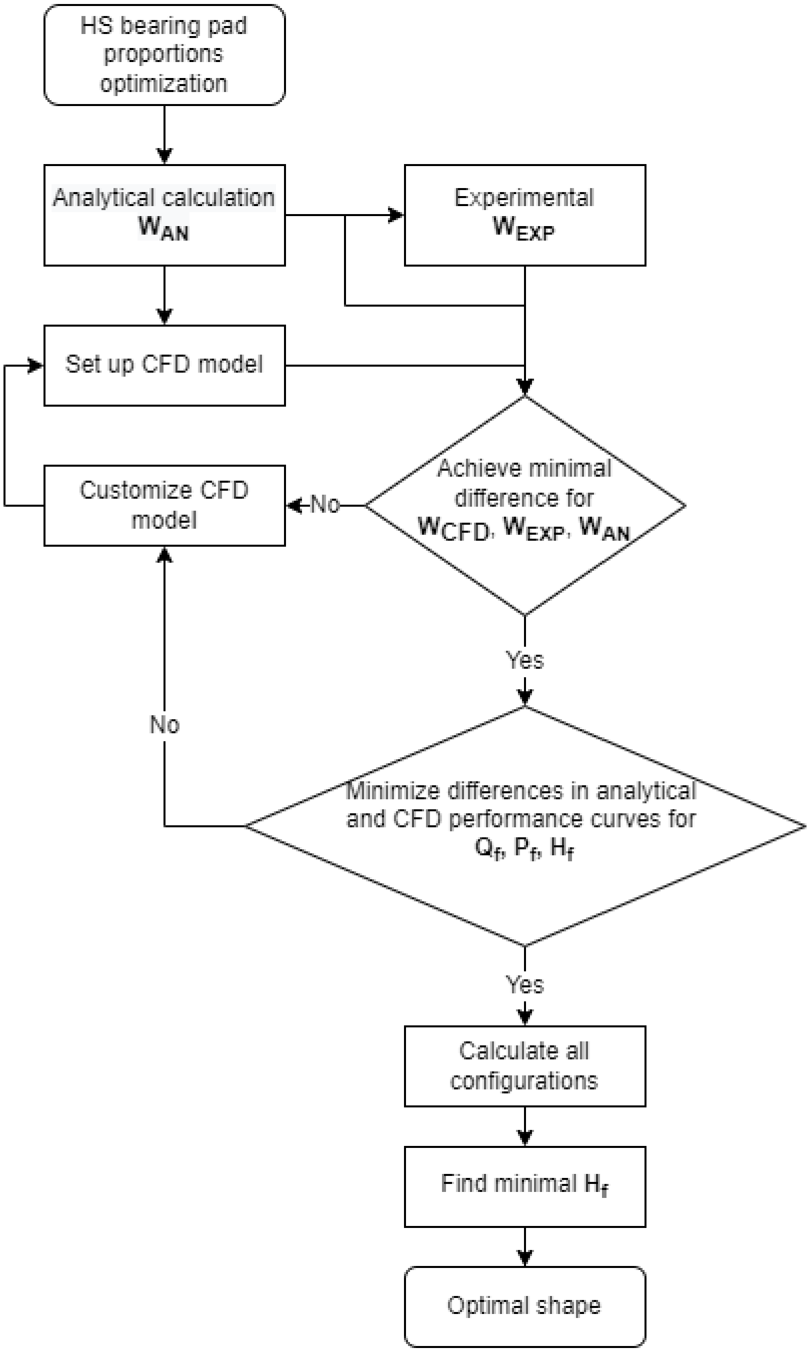

Figure 2

Optimization flowchart used in the presented study.

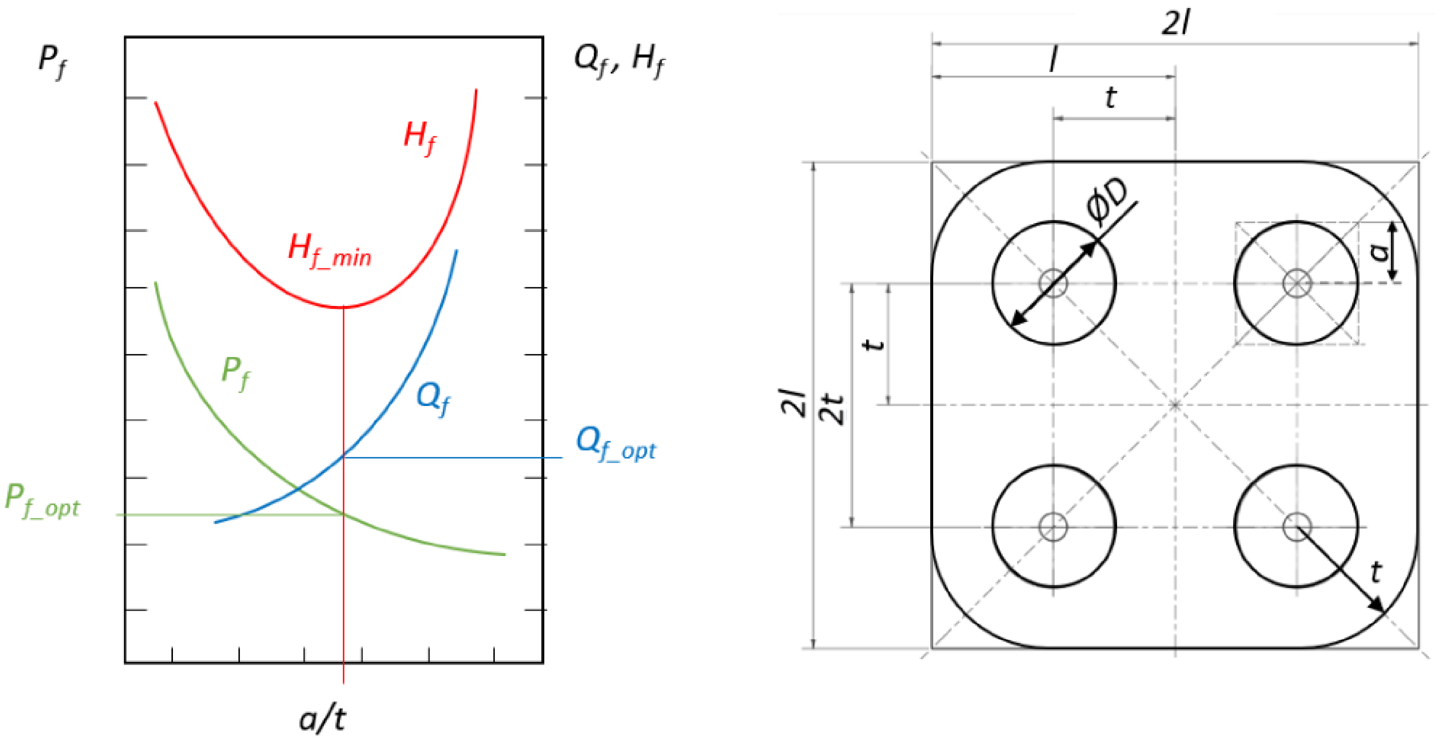

Figure 3

An example design chart using one-parameter optimization with geometry description from Loeb and Rippel [16]

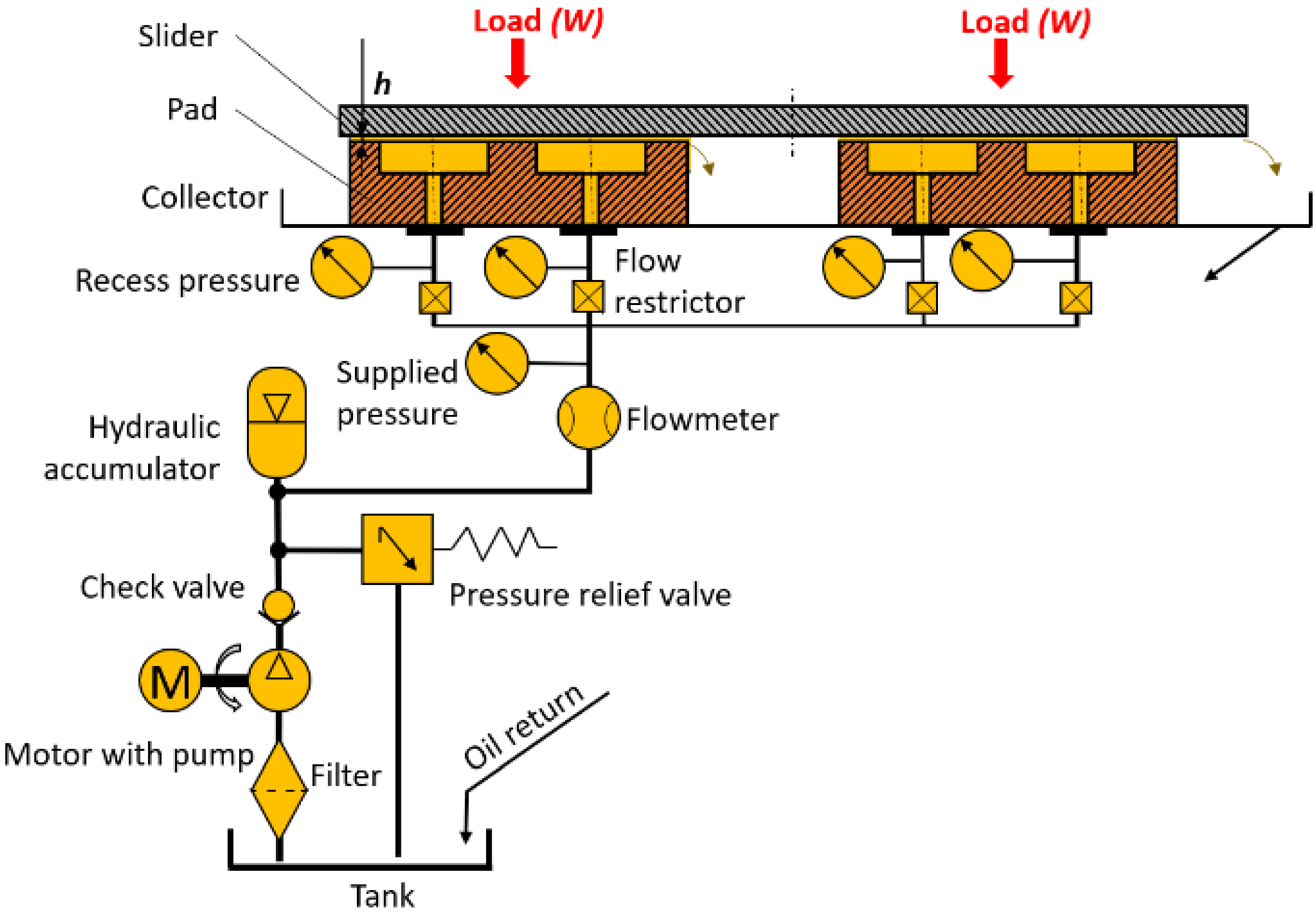

Figure 4

Schematic representation of 2-PAD experimental device

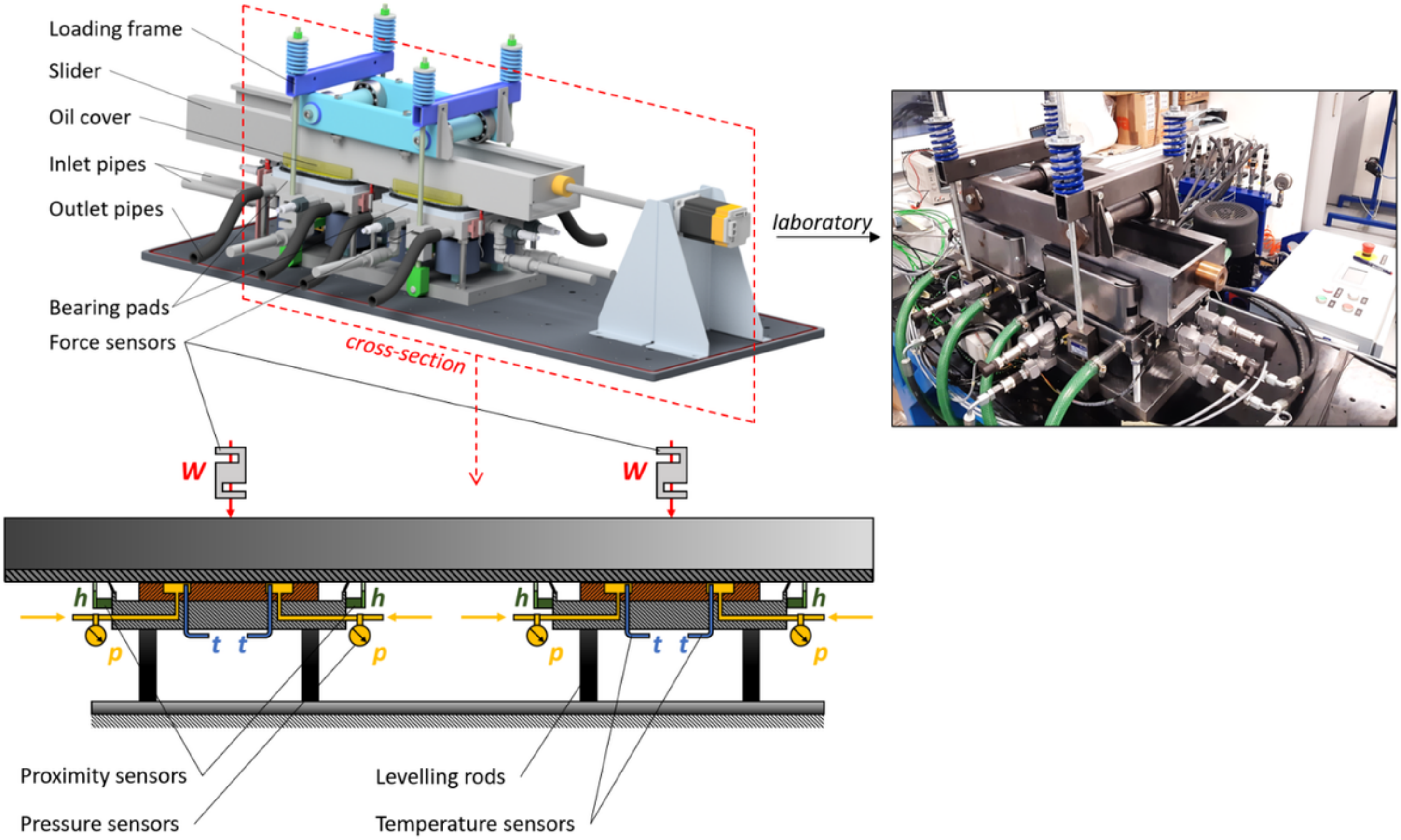

Figure 5

Schematical representation of the 2-PAD hydrostatic test bearing with sensor description and photography of the assembled experimental device in the laboratory.

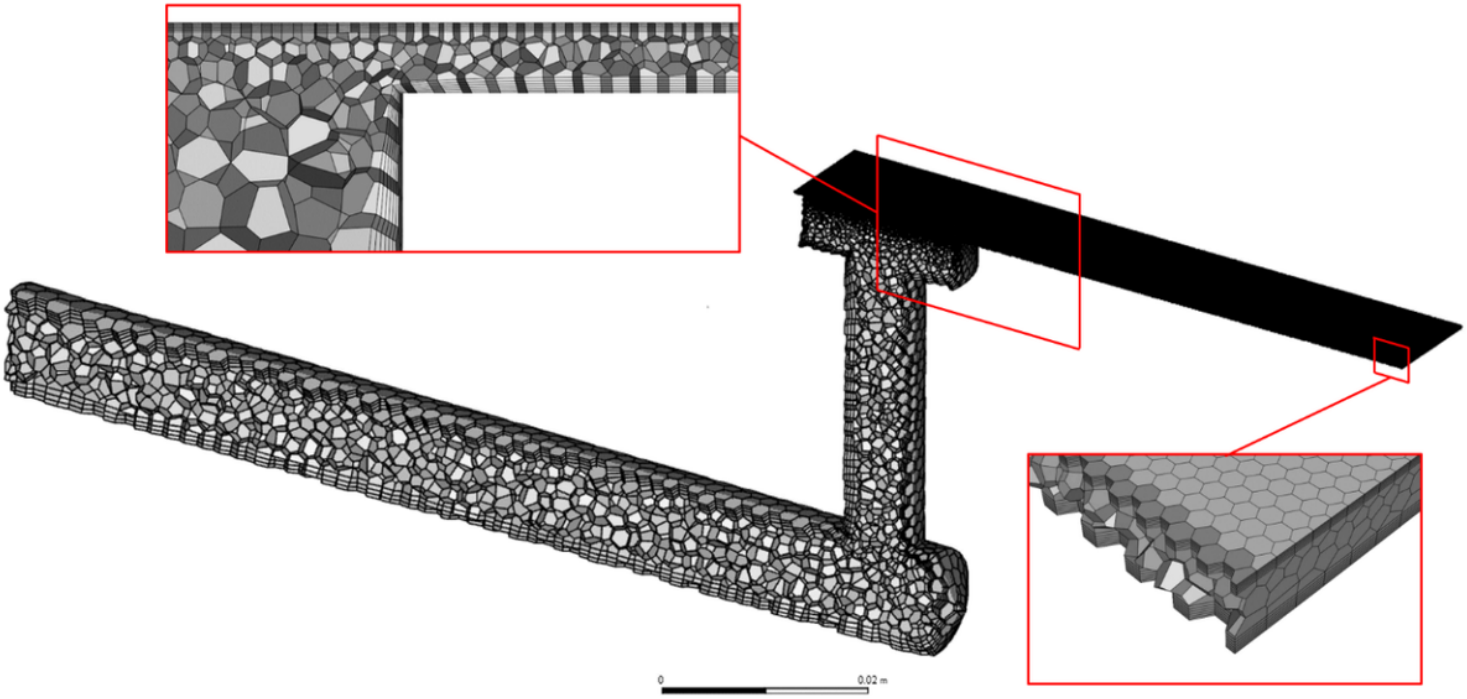

Figure 6

The discretized domain of one design point used for simulation with recess and lubricating film zones details.

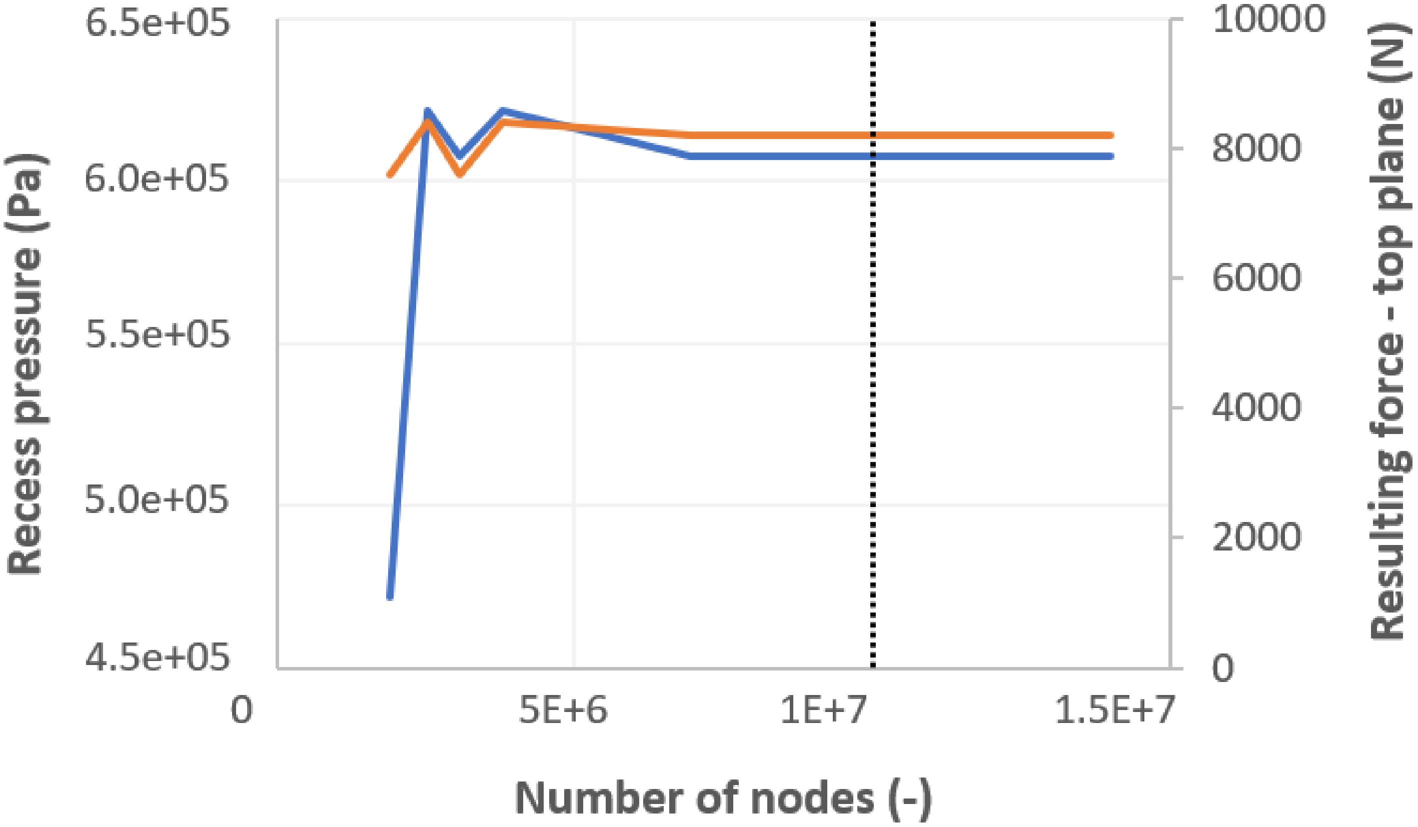

Figure 7

Mesh sensitivity analysis results.

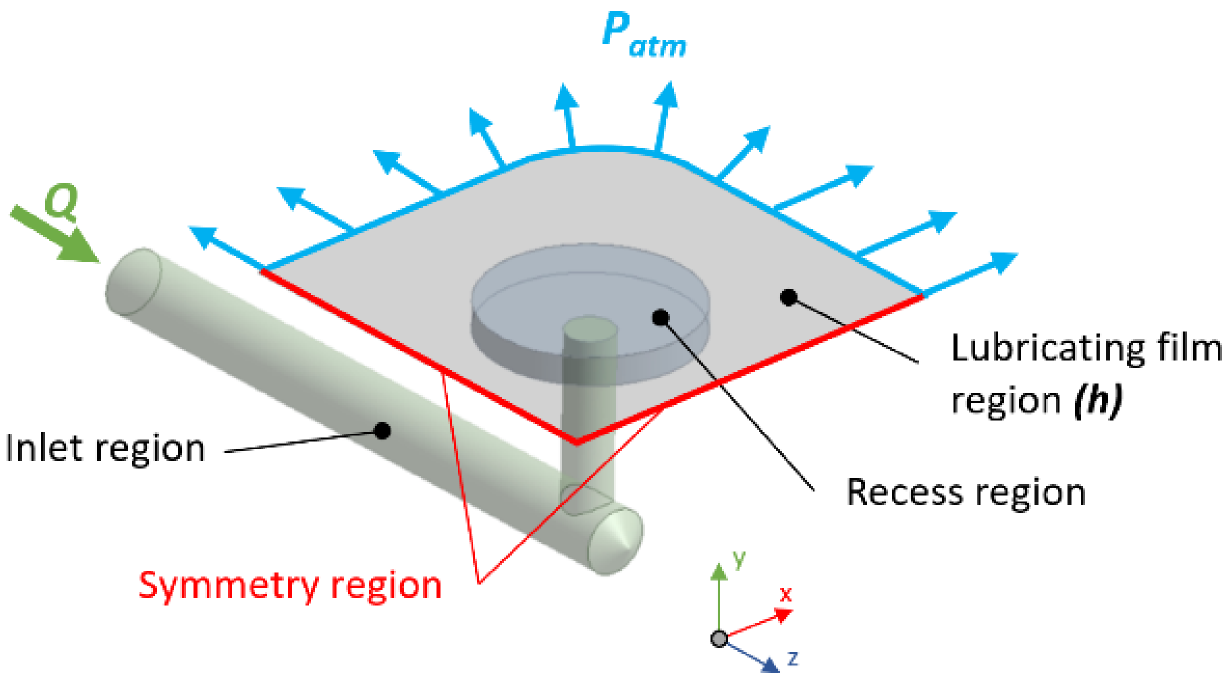

Figure 8

Quarter model with boundary conditions used for the CFD analyses.

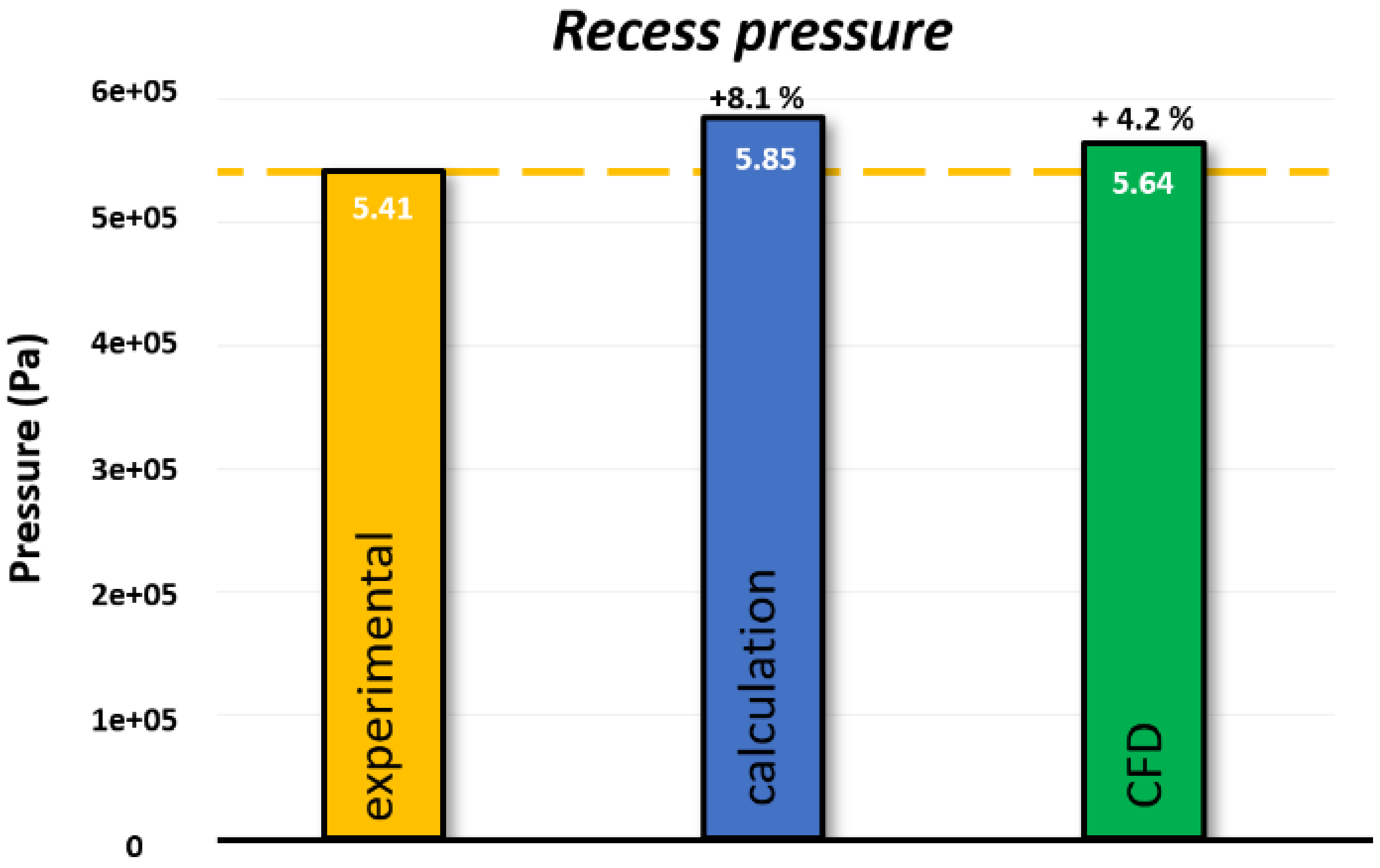

Figure 9

Recess pressure comparison obtained from experimental measurements, analytical calculation for the initial pad geometry.

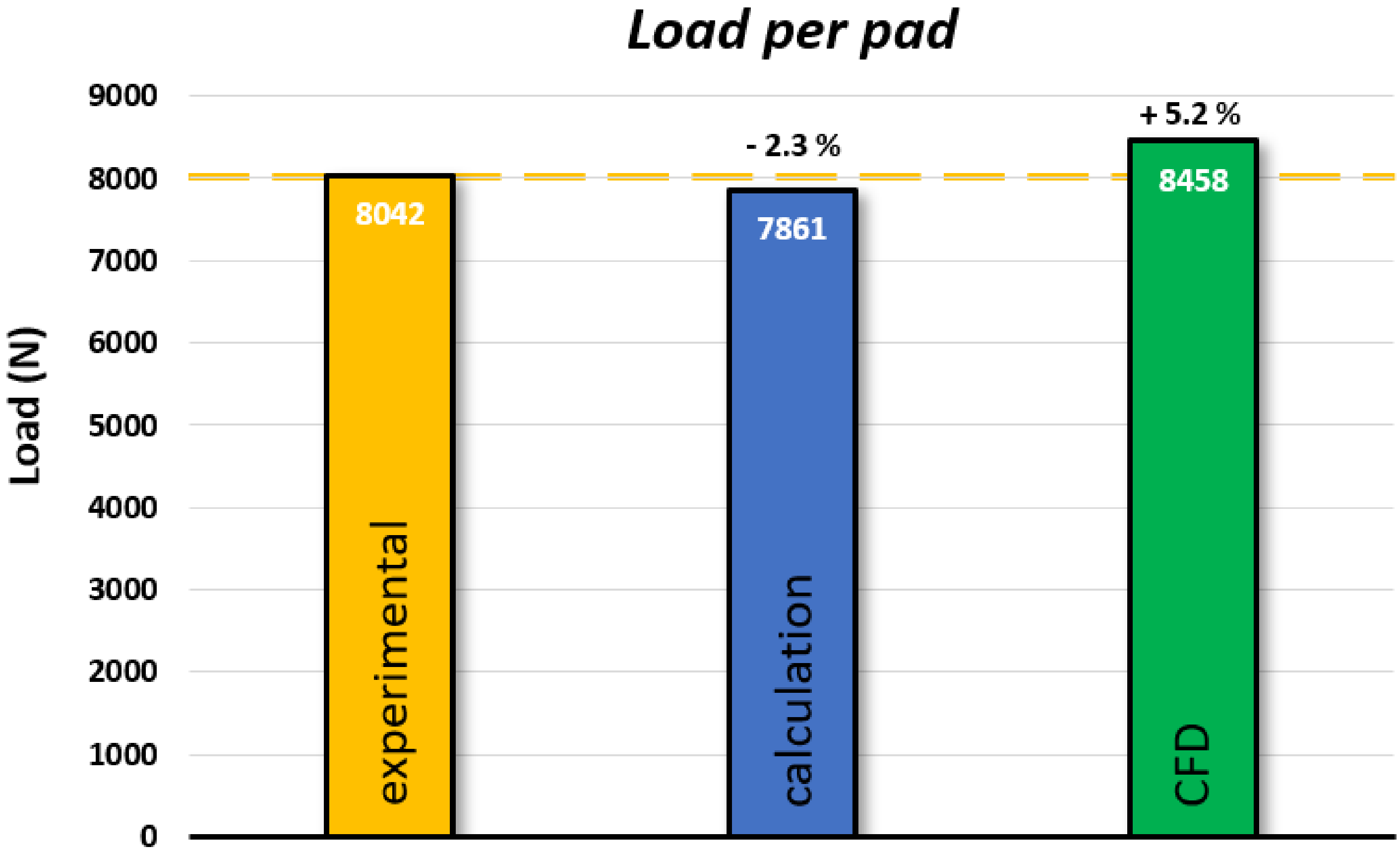

Figure 10

Load comparison obtained from experimental measurements, analytical calculation and CFD analysis for the initial pad geometry.

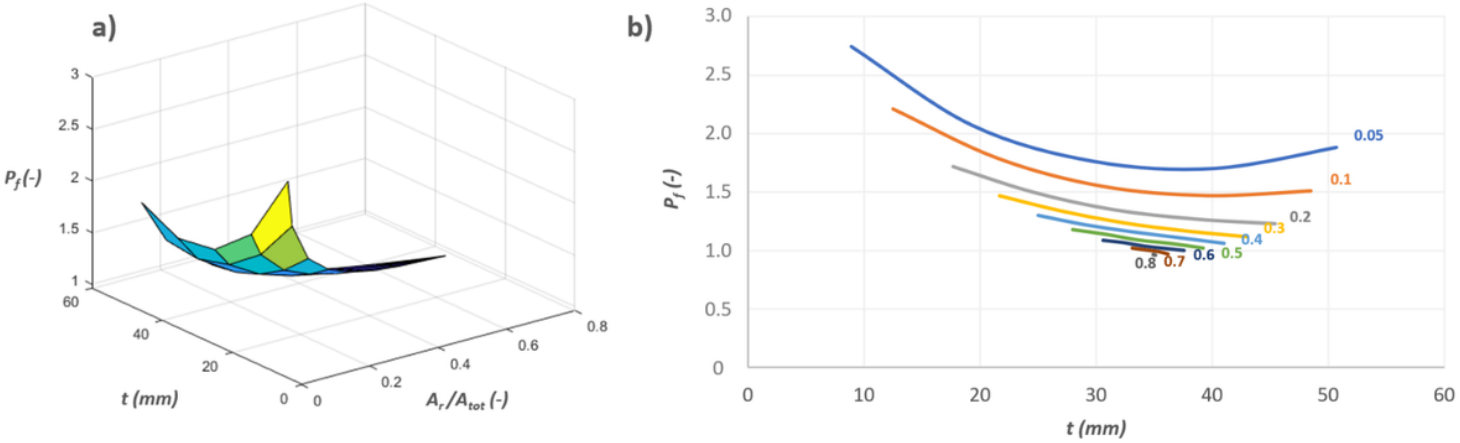

Figure 11

Load factor a) position and area ratio variation dependence and b) area ratio sections obtained from CFD analysis.

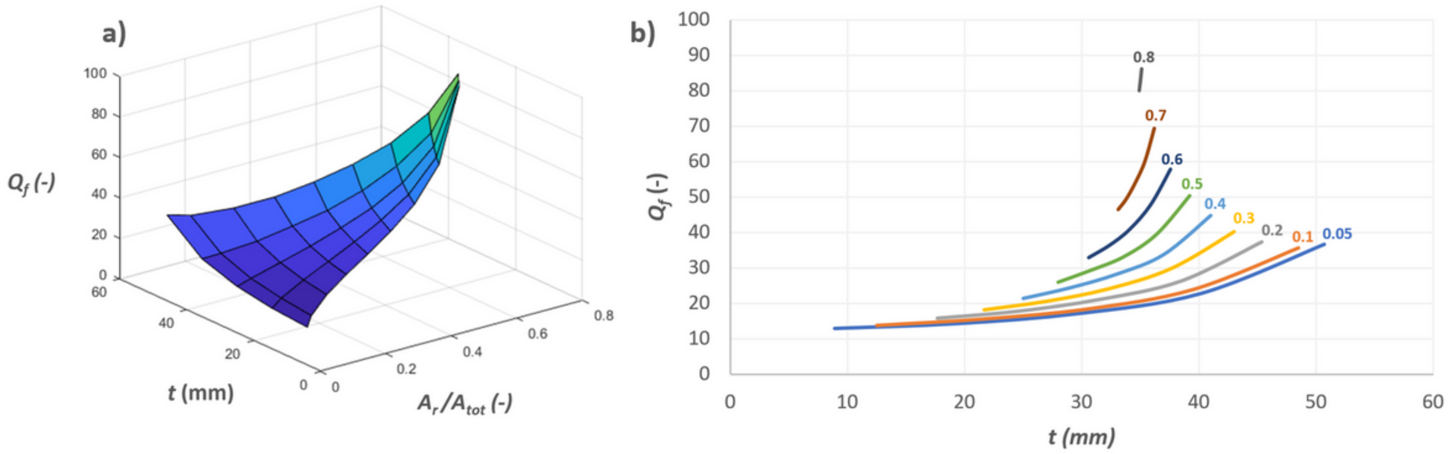

Figure 12

Flow factor a) position and area ratio variation dependence and b) area ratio sections obtained from CFD analysis.

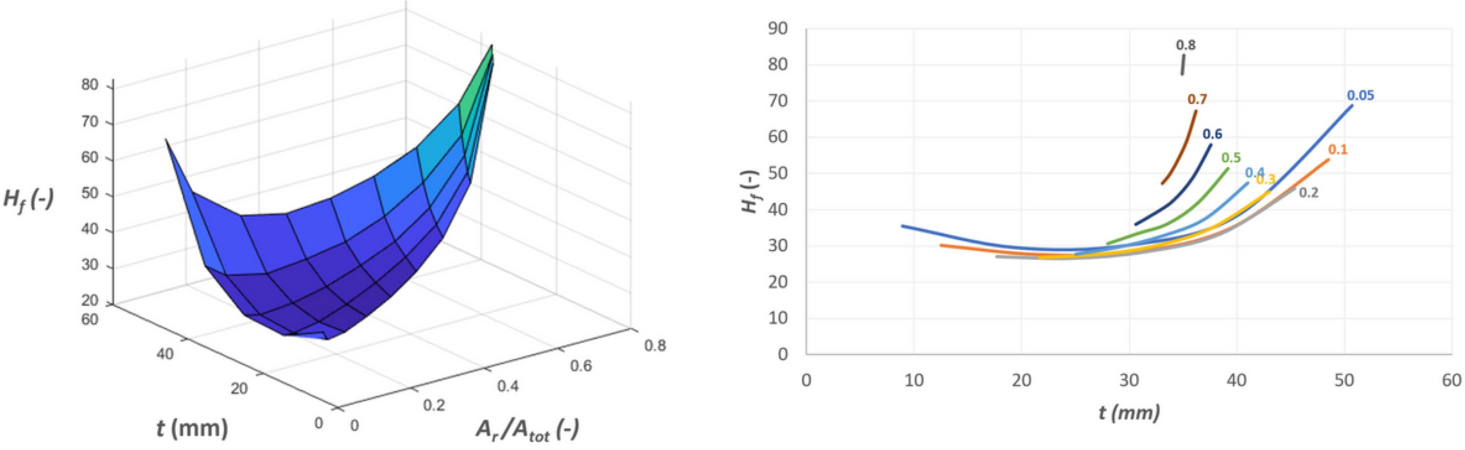

Figure 13

Power loss factor a) position and area ratio variation dependence and b) area ratio sections obtained from CFD analysis.

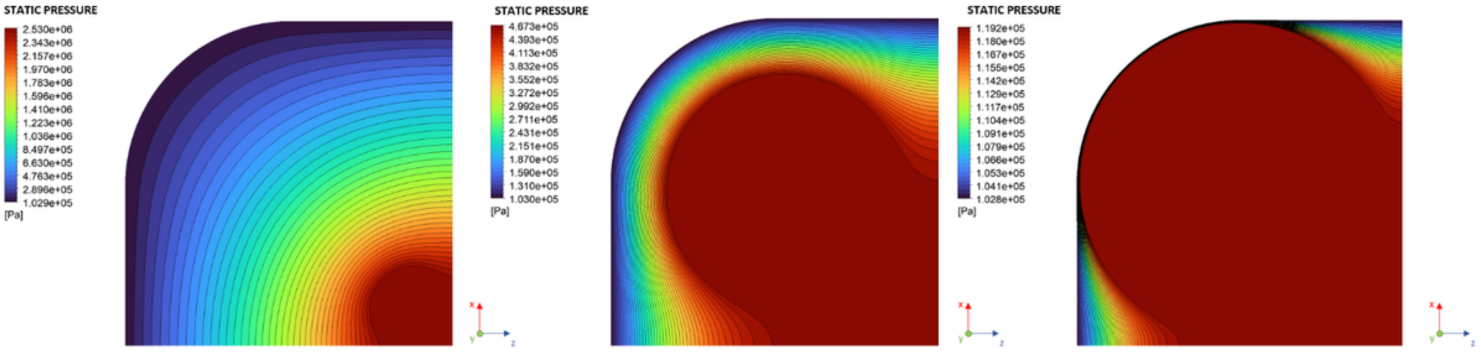

a) t=8.83; D=17.66

b) t=32.99; D=49.96

b) t=35.48; D=68.40

Figure 14

Top plane pressure contours of static pressure for recess size and position: a) smallest and closest to the centre, b) medium in the middle, and c) largest and farthest from the pad centre.

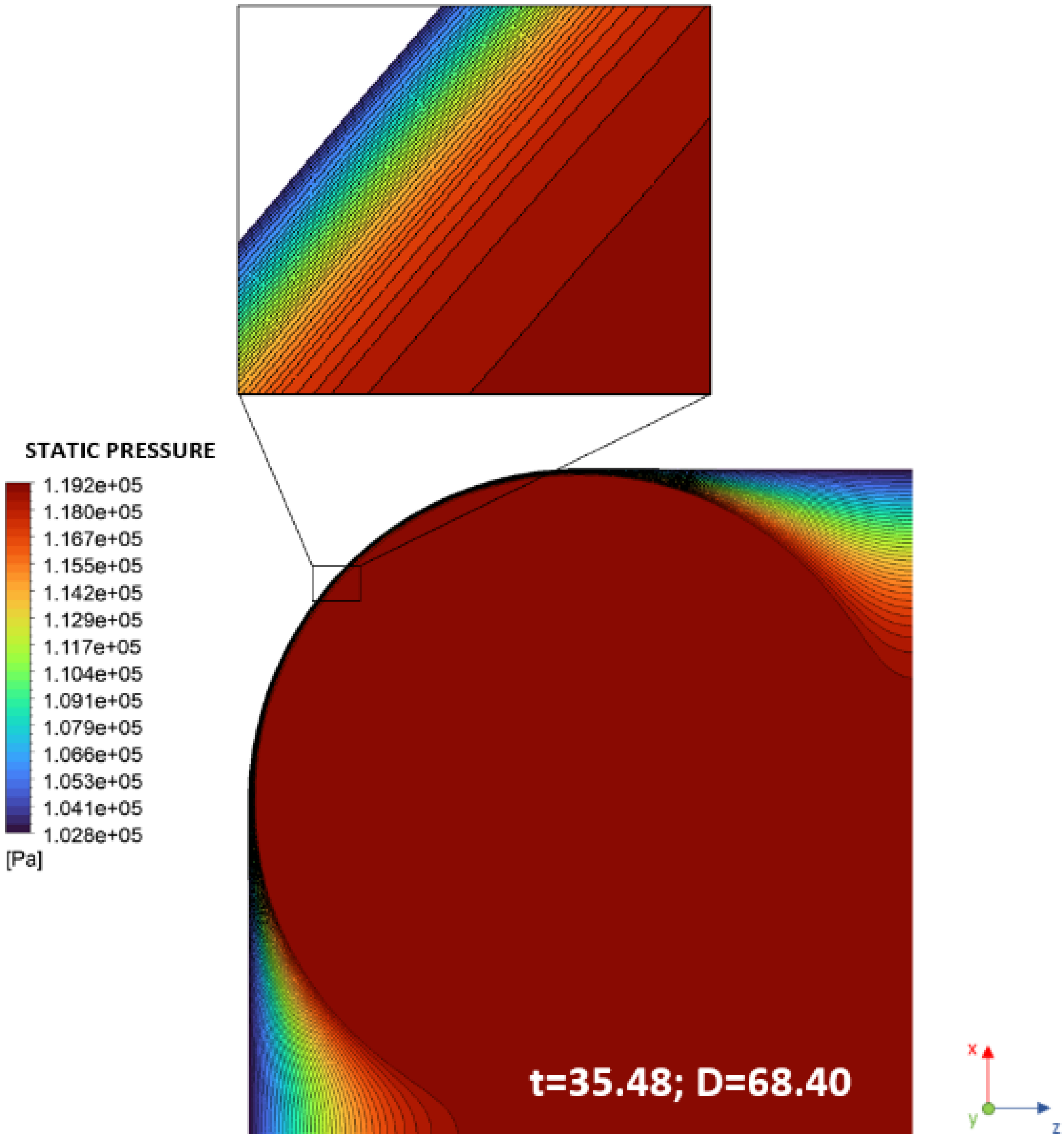

Figure 15

Top plane pressure contour of static pressure for recess size of 68.4 mm diameter and position 35.48 mm from the pad centre with detail on the sealing edge.

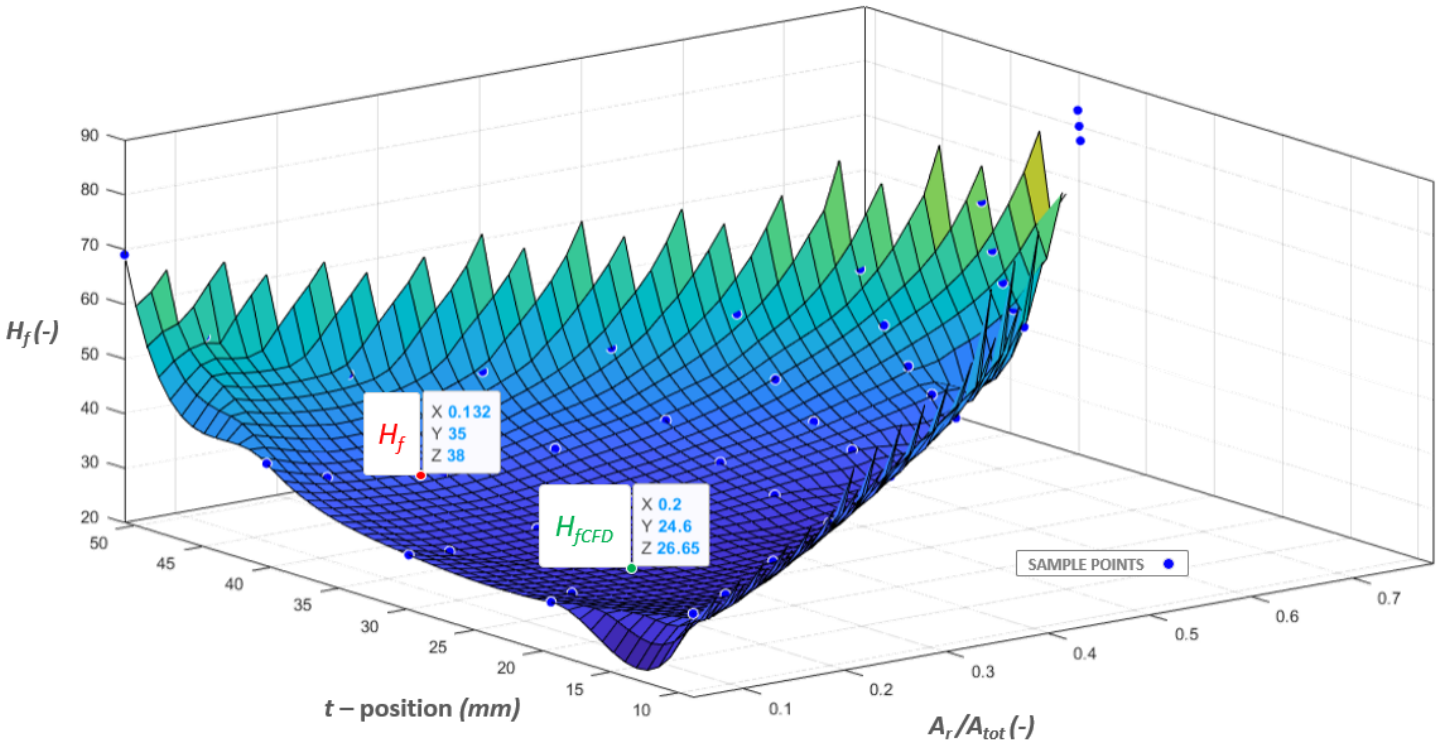

Figure 16

Power loss factor cubic interpolation of results obtained from CFD analysis with highlighted power loss factors obtained from [16].

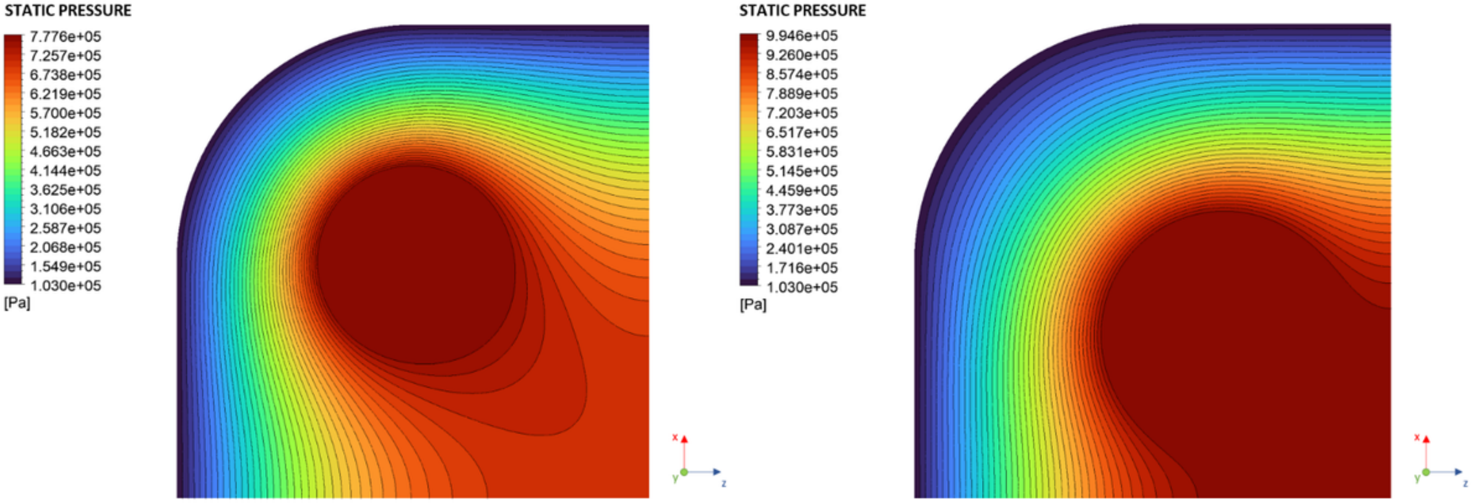

a) t=35.00; D=28.00

b) t=24.59; D=35.32

Figure 17

Top plane static pressure contours of optimized pad shapes using a) one-parameter approach and b) novel two-parameter approach.